

High Capacity Variable Friction Damper based on Band Brake Technology

Austin Downey^{a,d}, Liang Cao^a, Simon Laflamme^a, Douglas Taylor^b, James Ricles^c

^a*Department of Civil, Construction, and Environmental Engineering, Iowa State University, Ames, IA 50011, USA*

^b*Taylor Devices, North Tonawanda, NY 14120, U.S.A*

^c*Department of Civil and Environmental Engineering, Lehigh University, Bethlehem, PA 18015, U.S.A*

^d*Corresponding author, e-mail: adowney2@iastate.edu*

Abstract

Implementation of high performance controllable damping devices can ameliorate cost-effectiveness of structural systems for mitigation of natural hazards. However, the applications of these damping systems are limited due to a lack of 1) mechanical robustness; 2) electrical reliability; and 3) large resisting force capability. To broaden the implementation of modern damping systems, a novel semi-active damping device is proposed. The device, termed Banded Rotary Friction Device (BRFD), has enhanced applicability compared to other proposed damping systems due to its cost-effectiveness, high damping performance, mechanical robustness, and technological simplicity. Its mechanical principle is based on a band brake, which results in a high amplification of the applied force while enabling a variable control force. The theoretical model of the BRFD is presented and experimentally verified by subjecting a prototype to various harmonic loads. Results show that the prototype BRFD is capable of a maximum force of 45 kN (10 kips) using only

a 267 N (60 lb) actuation force, therefore providing a mechanical advantage of 169. A 3-stage dynamic model previously developed by the authors can successfully be used to model the dynamic behavior of the BRFD.

Keywords: Variable friction, semi-active device, structural control, vibration mitigation, supplemental damping, modified friction device

1. Introduction

Passive supplemental damping devices have become widely accepted in structural engineering for natural hazard mitigation [1, 2]. However, they are typically only applicable to a limited bandwidth of excitations because their damping forces cannot be varied post manufacturing. Active dampers are possible alternatives to provide higher mitigation performance. Nevertheless, they require large external power sources that may not be available during or after a natural hazard, have the potential to destabilize a system, and can be expensive to operate during sustained wind events [3].

Semi-active damping strategies combine some of the benefits of passive and active strategies [4]. They are purely reactive systems, in the sense that they cannot add energy to the control system, and can alter their mechanical properties to provide additional controllability using a fraction of the power required by active strategies. Semi-active devices are divided into four classes: variable stiffness [5, 6], variable orifices [7], variable fluid [8] and variable friction [9] devices.

19 In particular, variable friction devices are capable of high energy dissipa-
20 tion, independent of velocity by dissipating mechanical energy into heat via
21 a friction force that is controlled by an actuator with a varying normal force.
22 Examples of actuators used in variable friction devices include: pneumatic
23 [10, 11], hydraulic [12], electro-magnetic [13, 14], electro-mechanical [15, 16]
24 and piezoelectric [17, 18, 19, 20]. This controllability of the normal force
25 minimizes obstacles found in passive friction devices, namely, the response
26 produced by the strong nonlinear behavior, degradation of sliding interface,
27 and cold weld [21, 2].

28
29 Literature cites several examples of working variable friction prototypes
30 for structural control applications. A semi-active independently variable fric-
31 tion device possessing a 25 kN (5.5 kips) maximum damping force provided
32 by an electromechanical actuator has been experimentally verified [15]. Oth-
33 ers [18, 22] have investigated piezoelectric friction devices (PFD) of 0.5 kN
34 (2.2 kips) and 25 kN (5.5 kips) damping force capacity, respectively. An
35 electromagnetic friction damper device (EFD) having a 2.84 kN (0.64 kips)
36 damping force capacity has also been developed [23].

37
38 Despite these efforts to produce semi-active friction devices suited for
39 structural control applications, combined with studies demonstrating their
40 economic advantages over passive systems, (see [24, 25, 26]), their implemen-
41 tation has remained limited. This could be due to low damping capability
42 and the availability of mechanically reliable technologies [27].

43

44 In an effort to provide both high damping capacity and high mechanical
45 reliability, the authors have recently proposed a variable friction device based
46 on automotive dual servo drum brake technology. The technology, termed
47 the Modified Friction Device (MFD) was theoretically presented and a pro-
48 totype fabricated and demonstrated [27]. While the prototype was a small
49 scale version constructed from a 200 mm (8 in) automotive duo-servo drum
50 brake, a key feature found in the experimental verification was a discontinu-
51 ity of the friction dynamics when the rotation reversed due to the internal
52 layout of the braking shoes and bracing pins. This discontinuity led to a
53 sharp reduction in the damping force provided during a substantial portion
54 of a damping cycle. Under specific conditions of limited displacement, the
55 damper was found to provide very limited damping force, irrespective of the
56 applied force. The maximum damping force obtained from the prototype
57 was 3.1 kN (0.7 kip).

58

59 The objective of this paper is to introduce a second generation of rotary
60 variable friction devices with substantially enhanced applicability to mitiga-
61 tion of structural vibrations. This second generation device is designed to be
62 capable of producing a damping force of one order of magnitude higher while
63 overcoming the limitations found in the dynamics of the MFD and preserv-
64 ing a simple and mechanically robust design. This novel device, presented
65 for the first time, is based on band brake technology, and is termed Banded
66 Rotary Friction Device (BRFD). Band brakes have been used in mining and
67 marine mooring applications for decades [28, 29] and have proven to be a
68 mechanically robust technology [30]. Their maintenance costs are known

69 to be limited due to their simple mechanics, no internal parts or hydraulic
70 fluid, and the easy replacement/availability of friction material [31]. In this
71 paper, the BRFD is introduced, and a working prototype is experimentally
72 verified. The 3-stage dynamic model developed by the authors [27] is used
73 to characterize its behavior.

74 The paper is organized as follows. The next section introduces the BRFD
75 and provides its theoretical background. This is followed by a presentation of
76 a 3-stage dynamic model used in the characterization of the device's dynamic
77 behavior. The subsequent section discusses the experimental methodology
78 and the prototyping of the BRFD, along with a presentation and discussion
79 of the experimental results. The last section concludes the paper by provid-
80 ing a summary of the findings.

81

82 **2. Banded Rotary Friction Device**

83 The BRFD utilizes existing band brake technology. A band brake is a
84 robust and reliable friction brake consisting of a flexible band lined with fric-
85 tion material that tightens concentrically around a cylindrical drum to slow
86 or stop its rotation. The BRFD is a double band brake system, consisting of
87 a band lined with a friction material [31], doubled wrapped around a drum,
88 as shown in Fig. 1a. It is capable of providing variable braking torques as
89 a linear function of an applied force, which is significantly amplified by the
90 brake's positive servo effect.

91

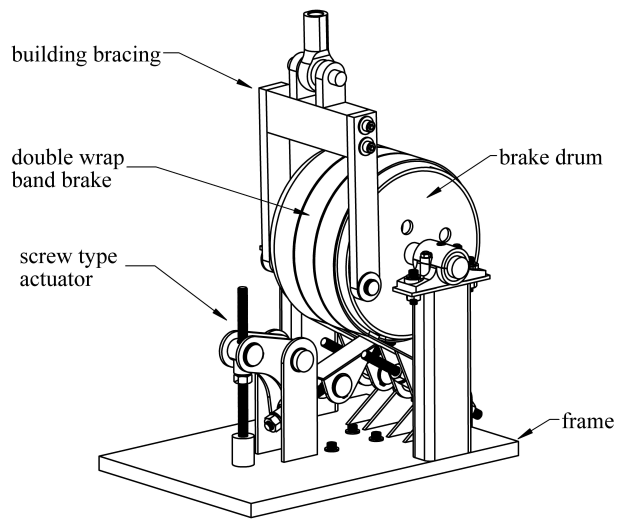
92 A 45 kN (10 kips) capacity prototype was fabricated based on the schematic

93 shown in Fig. 1a. The flat double wrap band is illustrated in Fig. 1b. The
94 band is lined with friction material and wrapped 670 degrees around the
95 circumference of the steel drum and anchored at both ends. The single end
96 of the band is attached to an actuation mechanism consisting of a threaded
97 rod for the purpose of varying the force applied to the band brake, and the
98 double end of the band is anchored to the rigid frame. The prototype has
99 been designed to be installed within a structural bracing scheme. Such an
100 implementation scheme is discussed below.

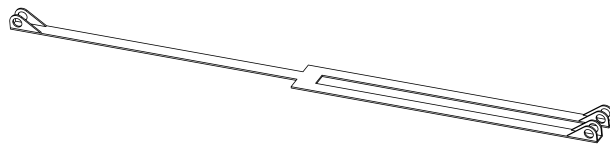
101

102 *2.1. Implementation within a Structural System*

103 The BRFD is designed to transform displacement into rotation, θ . The
104 device can therefore be integrated within a multiplicity of structural control
105 schemes, including hybrid base-isolation systems, semi-active tuned mass
106 dampers, and bracing elements. Fig. 2 shows the BRFD installed in two
107 possible configurations associated with a building lateral load resisting sys-
108 tem. Fig. 2(a) is a chevron system that transduces interstory drift δ into
109 rotation θ of the BRFD via the addition of a connecting link. Fig. 2(b) is a
110 toggle bracing configuration. The toggle bracing is used in structural motion
111 engineering to amplify the interstory drift [32]. While more expensive than a
112 typical chevron system, a toggle bracing system allows the BRFD to reach a
113 maximum frictional force faster and reduce the heat intensity on the friction
114 material, thus increasing the mitigation performance of the device. In both
115 configurations the inter story drift $\delta = x/H$, where x and H are the lateral
116 displacement of the floor and the story height, respectively. An expression
117 for the linear displacement y can be written as



(a) double wrap band brake system



(b) double wrap band brake

Figure 1: banded rotary friction device

$$y = \theta \cdot r_b \quad (1)$$

118 where r_b is the distance from the center of the drum to the brace connection.

119 For the chevron configuration where $y = x$ the rotation can be derived as

$$\theta = \frac{\delta \cdot H}{r_b} \quad (2)$$

120 For the toggle configuration, assuming small displacements, it can be
121 shown that [33]

$$y = \frac{\sin(\alpha)}{\cos(\alpha + \beta)} \cdot x \quad (3)$$

122 and

$$\theta = \frac{\sin(\alpha)}{\cos(\alpha + \beta)} \frac{\delta \cdot H}{r_b} \quad (4)$$

123 Eqs. (2) and (4) can be used in a performance-based design procedure [3].

124 The following section derives the equations governing the BRFD friction
125 mechanism.

126 *2.2. Friction Mechanism*

127 The friction force of the BRFD is generated by the drum rotating through
128 the stationary band. The band is anchored at one end (called the slack end),
129 where an input force (F_{applied}) is applied to the band, resulting in a reac-
130 tionary force (F_{reaction}) at the opposite end, as shown in Fig. 3. When rota-
131 tion of the drum is initiated, a friction force (F_{friction}) is generated opposing
132 the rotation of the drum at the interface between the friction material and
133 the drum. This force causes the band to experience an elastic deformation

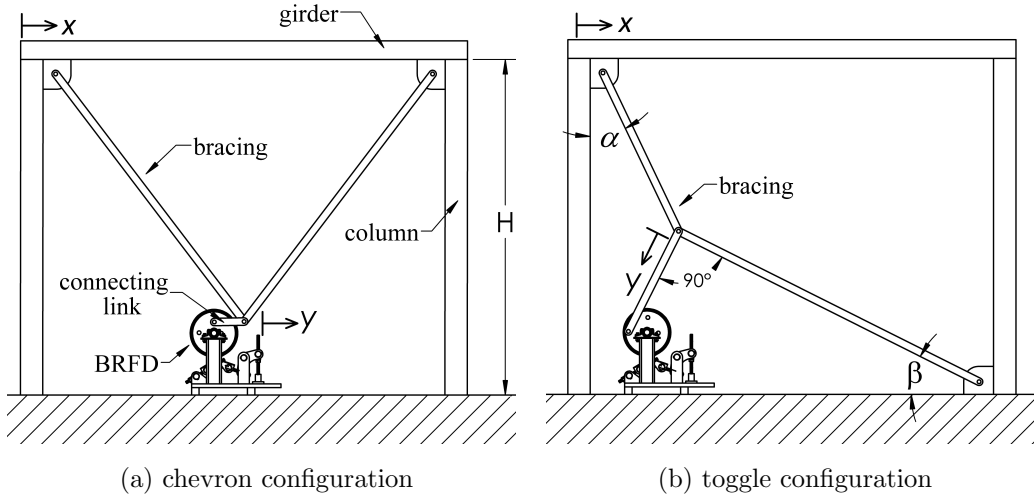


Figure 2: Two possible configurations for the BRFD installed within a building's lateral load resisting structural system.

134 and displacement in the direction of the drum rotation. The forces present
 135 in the band are expressed as, [34]

$$F_{\text{reaction}} = F_{\text{friction}} + F_{\text{applied}} \quad (5)$$

136 As the tension in the band increases towards the pinned end, the band
 137 wraps tightly around the drum, creating the positive servo effect, also known
 138 as the self-energizing effect. This phenomenon increases the contact pressure
 139 of the friction material linearly with respect to the angular displacement from
 140 the point of the applied force on the drum [34]. The continuously changing
 141 contact pressure between the band and the drum is shown in Fig. 3. The
 142 contact pressure increases uniformly from p_0 to p_{max} .

143

144 For the mathematical model it is assumed that the drum surface has a
 145 uniform curvature and the band conforms evenly to the drum surface. The
 146 initial asymmetry due to the elastic deformation of the band material is not
 147 considered. The forces F_{applied} , F_{reaction} and F_{friction} can be related to each
 148 other as follows. The relationship between the forces acting on the band ends
 149 (F_{applied} and F_{reaction}) is expressed as

$$F_{\text{reaction}}/F_{\text{applied}} = e^{\mu\phi} \quad (6)$$

150 where ϕ and μ represent the band wrap in radians and the friction coefficient
 151 of the friction material, respectively. Equations 5 and 6 can be combined to
 152 show

$$F_{\text{reaction}} = \frac{F_{\text{friction}} \cdot e^{\mu\phi}}{(e^{\mu\phi} - 1)} \quad (7)$$

$$F_{\text{applied}} = \frac{F_{\text{friction}}}{(e^{\mu\phi} - 1)} \quad (8)$$

153 It can be noted from Eq. (5) that the friction force F_{friction} is independent
 154 of the drum radius r . However, a braking torque T can be expressed as
 155 $T = F_{\text{friction}} \cdot r$. This braking torque is used to generate a damping force,
 156 F_{damping} ,

$$F_{\text{damping}} = \frac{T}{r_b} = \frac{F_{\text{friction}} \cdot r}{r_b} \quad (9)$$

157 where F_{damping} is the force applied to the bracing element. From Eq. (9), the
 158 device's mechanical advantage C is derived as:

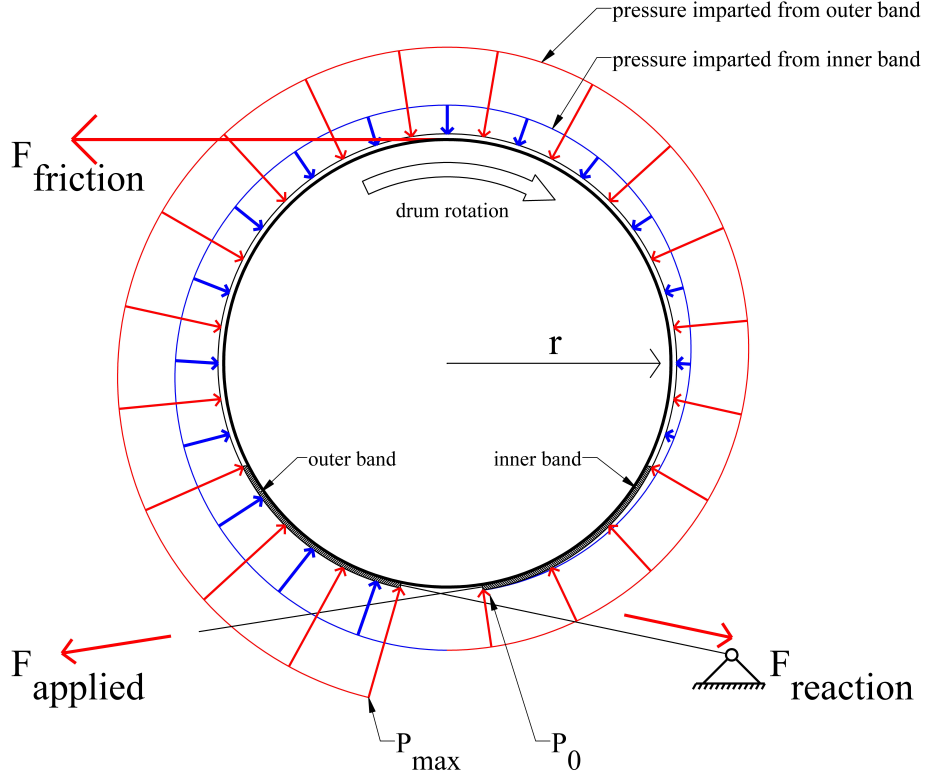


Figure 3: Forces acting on the BRFD

$$C = \frac{F_{\text{damping}}}{F_{\text{applied}}} = (e^{\mu\phi} - 1) \cdot \left(\frac{r}{r_b}\right) \quad (10)$$

159 where $F_{\text{damping}} > F_{\text{applied}}$ [35]. The mechanical advantage C is a function
 160 of the constants ϕ (expressed in radians), μ , r and r_b , which are determined
 161 during the device's design process. It follows that F_{damping} is a linear response
 162 of F_{applied} amplified by the constant C .

163

164 A schematic of the side view of the BRFD is shown in Fig. 4, where forces
 165 w_1 and w_2 can be either (F_{applied}) or (F_{reaction}) depending on the direction of

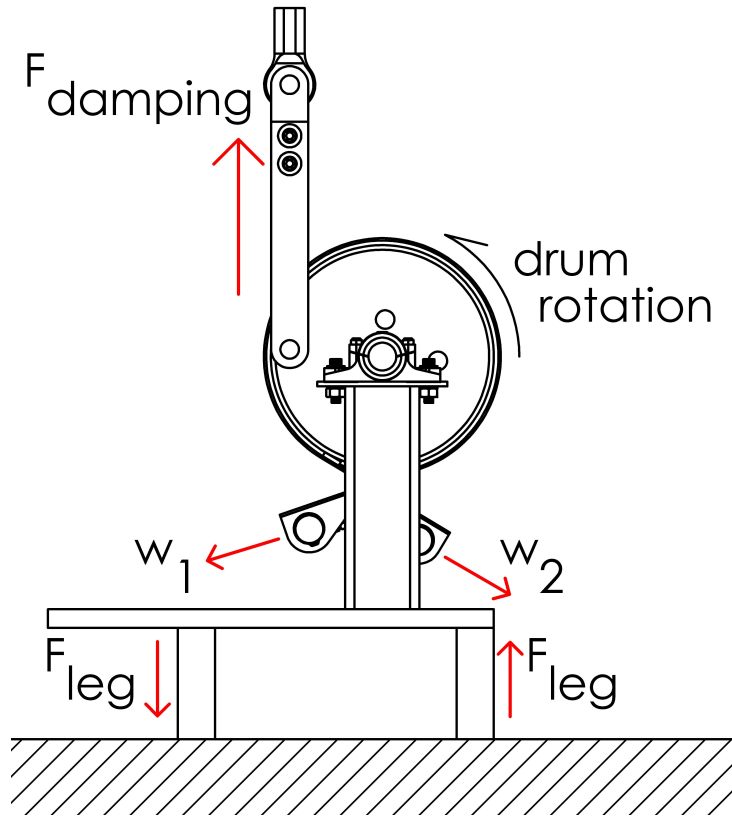


Figure 4: Schematic of the side view of the BRFD

166 rotation of the drum. This design implementation allows for the damper to
 167 take advantage of the positive servo effect in both directions of rotation. The
 168 BRFD is designed to sit on two support legs that produce opposite forces F_{leg}
 169 that counteracts the moment produced by the friction forces on the drum.

170 3. Dynamic Model

171 The authors have previously proposed a 3-stage dynamic model based on
 172 a modified LuGre model [27] for characterizing the friction behavior of the
 173 first generation of a rotary damping device (i.e., the MFD). This particular

174 dynamic model was useful at characterizing the drop in force that occurs
175 when the rotation of the drum is reversed. As it will be observed in the
176 experimental results presented herein, the BRFD still exhibits a small drop
177 in force upon reversal and the 3-stage dynamic model therefore still applies.
178 This can be observed in Fig. 5 under “stage 2”. This drop in the force is a
179 product of the rearrangement of the device’s components and forces caused
180 by the change in direction of the brake drum, termed backlash. Four major
181 sources of backlash in the BRFD prototype are as follows:

- 182 1. Elastic deformation of the band that occurs during the initial drum
183 rotation.
- 184 2. Deviations of the band from an ideal uniform curvature encasing the
185 drum, causing non-uniformed strain in the metal band;
- 186 3. Excess curvature present were the band connects to the supporting link-
187 age. The curvature of the band in the connecting region changes when
188 the force changes from (F_{applied}) to (F_{reaction}), resulting in a changing
189 chord length. This phenomenon can be seen in Fig 7.
- 190 4. Deflection of the base and legs supporting the rotating drum.

191 The 3-stage dynamic model allows for the accurate modeling of the hys-
192 teretic behavior, including the stiffness region developed by the BRFD’s back-
193 lash. Fig. 5 illustrate the three different stages through a plot of a typical
194 dynamic response of the BRFD extracted from the experimental results un-
195 der a harmonic displacement input of 25.4mm (1 in) amplitude, divided into
196 3 stages:

- 197 • Stage 1 (location 1 \rightarrow location 2) - The system is in a typical dynamic
198 friction mode. The friction force associated with this stage, (F_1), is
199 characterized using a LuGre friction model. This stage occurs until
200 rotation is reversed and the frictional force is lost.
- 201 • Stage 2 (location 2 \rightarrow location 3) - The linear force F_2 , associated with
202 Stage 2 is characterized as being proportional to a stiffness element k_2 .
203 This stage occurs over a drum displacement d_2 . The length of this stage
204 is governed by the amount of backlash present in the device.
- 205 • Stage 3 (location 3 \rightarrow location 1) - The force F_3 associated with this
206 stage is characterized as being proportional to a stiffness element k_3 .
207 This stage occurs over a drum displacement d_3 , after the backlash gap
208 has been taken up by the rotating drum.

209 The LuGre friction model was selected to characterize the device's friction
210 mode due to its capacity to model the stick-slip motion and the Stribeck effect
211 [36]. The LuGre model has been applied to a wide range of systems due to
212 its computational simplicity [37, 38, 39, 40]. Under this model, the friction
213 force is written

$$F_{\text{friction}} = \sigma_0 z + \sigma_1 \dot{z} + \sigma_2 \dot{\zeta} \quad (11)$$

214 where,

$$\dot{z} = \dot{\zeta} - \sigma_0 \frac{|\dot{\zeta}|}{g(\dot{\zeta})} z \quad (12)$$

215 where σ_0 is a constant representing the aggregate bristle stiffness, σ_1 is the
216 microdamping, σ_2 is the viscous friction, z is an evolutionary variable, $\dot{\zeta}$ is

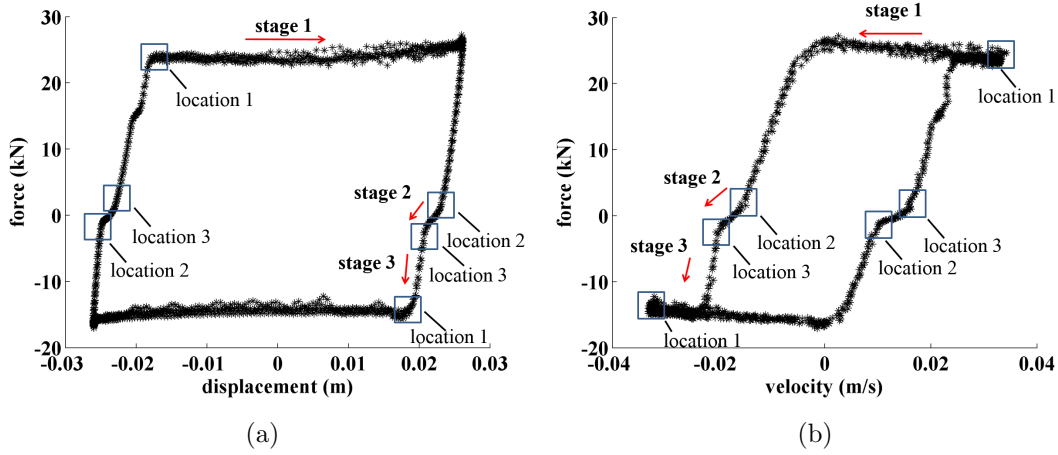


Figure 5: Dynamic response of the BRFD under applied force of 133 N (30 lb) : (a) force-displacement hysteretic response (0.2 Hz); and (b) force-velocity hysteretic response (0.2 Hz).

217 the BRFD's surface displacement and velocity, and $g(\dot{\zeta})$ is a function used
 218 to describe the Stribeck effect

$$g(\dot{\zeta}) = F_c + (F_s - F_c)e^{-\left(\frac{\dot{\zeta}}{\dot{x}_s}\right)^2} \quad (13)$$

219 where \dot{x}_s is a constant representing the Stribeck velocity, F_s is the static
 220 friction force, and F_c the kinetic friction force. F_s is taken when the velocity
 221 of the device $\dot{\zeta} = 0$, and F_c taken as the steady state force (when $\dot{\zeta} \gg \dot{x}_s$).
 222 In Eq. (10), $\zeta \approx \theta \cdot r$.

223 A smoothing function is introduced to the transition region between each
 224 dynamic stage. It consists of a C^∞ function of the following type [41]:

$$m(\zeta) = \frac{1}{1 + e^{-\frac{\gamma_1(\zeta - \zeta_0)}{\gamma_2}}} \quad (14)$$

225 where ζ_0 is the reference displacement of the new stage, and γ_1, γ_2 are con-
226 stants. For instance, the total force F during the transition from stage i to
227 stage j is written

$$F = (1 - m(\zeta))F_i + m(\zeta)F_j \quad (15)$$

228 where $F_{i,j}$ is the total force computed using the definition of stage i, j . Re-
229 mark: the amplitude of the damping force of the prototype is not symmetric
230 as a function of the rotational direction. This can be explained by the asym-
231 metries in the friction material and band. A proper break-in procedure should
232 significantly reduce or eliminate the unsymmetrical damping dynamics. This
233 is out-of-the-scope of this paper. Here, the static and dynamic friction force
234 coefficients are separated between forward ($F_{s,\text{fwd}}$ and $F_{c,\text{fwd}}$) and backward
235 ($F_{s,\text{bwd}}$ and $F_{c,\text{bwd}}$) force components.

236

237 4. Experimental Validation

238 4.1. Prototype

239 A prototype of the BRFD from the schematic shown in Fig. 1a was fab-
240 ricated to verify its performance at producing high damping forces. Friction
241 material used was flexible, asbestos-free, woven yarn material with copper
242 wire [31]. The design parameters are listed in Table 1. A photograph of the
243 prototype is shown in Fig. 6.

244 4.2. Methodology

245 The prototype BRFD was mounted in a servo-hydraulic testing machine
246 and its characterization performed. Applied forces were controlled through

Table 1: Design parameters of the BRFD prototype

Parameter	Value
Drum diameter	0.30 m (12 in)
Damping radius (r_b)	0.10 m (4 in)
Drum material	A-53 steel
Total band brake length	2.13 meters (84 in)
Band thickness	3.2 mm ($1/8$ in)
Band material	A-36 steel
Friction material	Woven, asbestos-free
Coefficient of friction (μ)	0.39
Band brake wrap (ϕ)	670°
Mechanical advantage (C)	142



Figure 6: BRFD testing setup

247 a screw-activated tensioner attached to one side of the band. A load cell
248 was placed between the BRFD's frame and the activation mechanism for
249 measuring the applied forces. The damping force generated by the BRFD
250 was measured via a load cell located in the head of the testing machine.
251 The test setup is shown in Fig. 6, with the BRFD in its fully un-actuated
252 position. The testing of the BRFD was limited to its designed 45 kN (10
253 kips) damping force capacity.

254 The prototype was subjected to displacement-controlled harmonic exci-
255 tations of 25.4 mm (1 in) amplitude at four different frequencies: 0.05, 0.1,
256 0.2, and 0.5 Hz. Five different applied forces (F_{applied}) were investigated: 35

257 (8), 53 (12), 66 (15), 133 (30) and 267 N (60 lbs), where 35 N (8 lbs) is the
258 minimum force available from the actuation mechanism and 267 N (60 lbs)
259 corresponds approximately to the prototypes maximum capacity. A total of
260 20 tests were performed.

261

262 4.3. Model Parameters

263 The 3-stage dynamic model parameters were identified by minimizing the
264 performance function J , consisting of the fitting error between the estimated
265 force from the model $\hat{F}_{\text{friction}}$ and experimental data F_{friction} for each test k :

266

$$J_k = \|\hat{F}_{\text{friction},k} - F_{\text{friction},k}\|_2 \quad (16)$$

267 where $\|\cdot\|_2$ is the 2nd Euclidean norm. This minimization was conducted in
268 MATLAB by using the command `fminsearch` under various arbitrary (and
269 physically realistic) initial conditions. Model parameters dependent on the
270 applied force (F_{applied}) are the static friction F_s , the dynamic friction F_c , and
271 the aggregate bristle stiffness σ_0 .

272

273 Table 2 lists the average values of the applied force dependent model
274 parameters, obtained from the experimental results. These average values
275 exhibit a linear and amplified response to the applied forces. This linearity
276 would typically be modeled and used in a model fitting task. However, due to
277 the medium fidelity of the developed prototype, test results experienced some
278 irregularities. These irregularities are likely caused by deviations of the band

Table 2: applied force dependent model parameters

Parameter	F_{applied}				
	35 N	53 N	66 N	133 N	267 N
$F_{c,\text{fwd}}$ (kN)	0.805	1.91	13.3	22.7	37.3
$F_{c,\text{bwd}}$ (kN)	0.538	0.521	3.11	13.4	37.8
$F_{s,\text{fwd}}$ (kN)	0.894	2.23	14.2	23.6	39.1
$F_{s,\text{bwd}}$ (kN)	0.619	0.579	3.33	14.2	44.5
σ_0 (kN·m ⁻¹)	525	613	1490	5694	9198

279 from an ideal uniform curvature, and bending in the BRFD's frame. These
 280 constraints are not inherent to the devices' architecture and would be elimi-
 281 nated in a high fidelity prototype or production model. With the current dis-
 282 crepancies and the relatively low number of characterization tests performed,
 283 a linear fit of the results produces a high level of error on the estimation of
 284 the parameters. Therefore, a function of the type $F_{(c,s),(fwd,bwd)} = f(F_{\text{applied}})$
 285 is out of the scope of this work.

286

287 The mechanical advantage C can be directly calculated by using F_c values
 288 from Table 2 as F_{damping} in Eq. (10) . However, given the variability in
 289 the data explained above, there would be an important variability in the
 290 experimental C computed for each test. To serve as a preliminary comparison
 291 with theory, it is best to use the values at the highest level of the applied
 292 forces, for which the band brake is the tightest and its angle is the most
 293 constant. For instance, Fig. 7 shows the changing band tension for applied

294 forces of 35, 66, and 267 N. The change in force results in a change in the
 295 gap between the friction material on the bands and the drum, this changing
 296 distance is exhibited in Fig. 7a through Fig. 7c. These changes are a function
 297 of the forces applied to the band. These frames were taken while the drum
 298 was in a backwards (clockwise) rotation, where the two exterior bands are
 299 acting as the fixed or reactionary ends.

300 Table 3 list the C values for the forward rotation (C_{fwd}) and backward
 301 rotation (C_{bwd}) of the drum, along with the experimental friction coefficient
 302 μ derived using Eq. (10) for both rotational directions. The experimental
 303 results show an agreement with the design value of C and the materials prop-
 304 erties provided by the manufacturer (μ). The lower C value for the backward
 305 rotation may be attributed to the asymmetries in the metal band and the
 306 adhered friction material.

307

Table 3: Validation of design parameters

Parameter	test value	design value
C_{fwd}	145	142
C_{bwd}	126	142
μ_{fwd}	0.42	0.39
μ_{bwd}	0.41	0.39

308 4.4. Assessment of Model Accuracy

309 Fig. 8 and 9 show plots of the experimental data fitting with the 3-stage
 310 model for 0.05 and 0.50 Hz excitations, respectively, under various levels

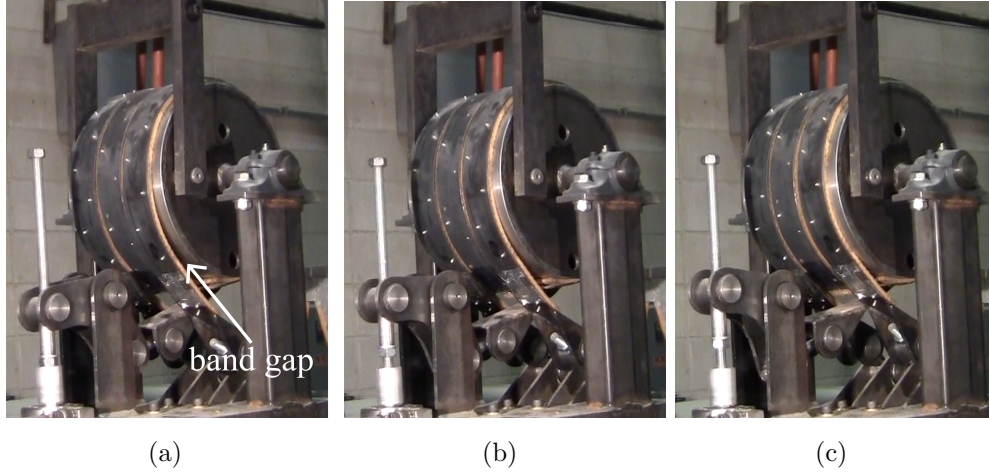


Figure 7: Band gap varying with the applied forces, (a) 35 N; (b) 66 N ; (c) 267 N;

311 of F_{applied} (35, 53, 66, 133, and 267 N). The model shows good agreement
 312 with the experimental data for all of the applied forces. There is a loss in
 313 fitting performance at the higher frequencies due to chattering in the device.
 314 Another observation in the 0.50 Hz excitation data is an unmodeled hump
 315 that occurs with a change in the rotational direction of the brake drum, for
 316 the case of a maximum applied force (267 N), and is less apparent at 133
 317 N. This hump is likely due to slippage of the the friction material due to
 318 deviations in the brake band. Fig. 10 compares the responses under various
 319 excitation frequencies under a 133 N applied force. Results are typical of
 320 other applied forces. The model shows good agreement with the experiment
 321 data for all frequencies, with a decrease in the fitting performance at the
 322 larger frequencies. This is consistent with the previous results.

323 Table 4 reports the root mean square error (RMSE) between the model
 324 prediction and experimental data results. Results are also compared with a

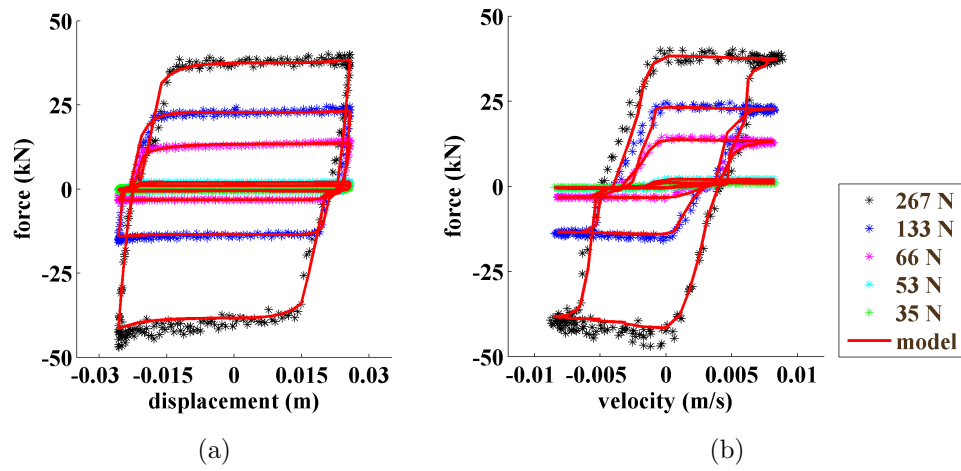


Figure 8: Experimental data fitting under various levels of applied forces for a 0.05 Hz excitation: (a) force-displacement; (b) force-velocity plots.

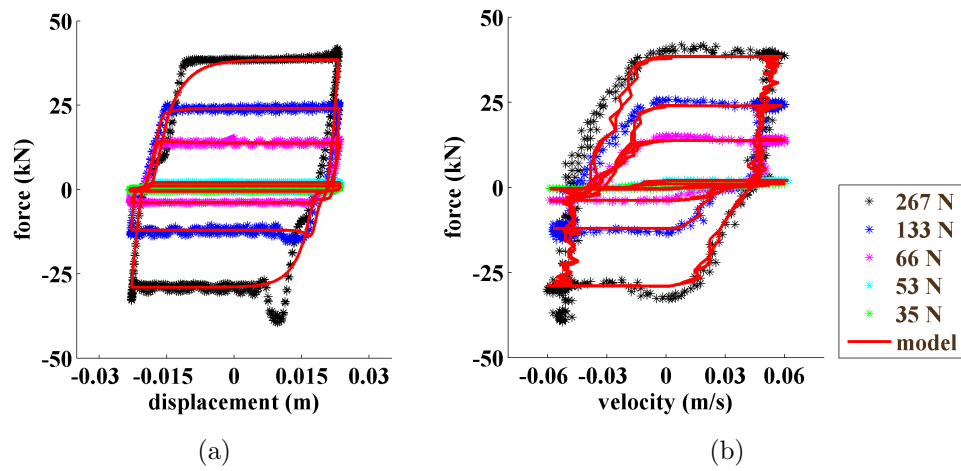


Figure 9: Experimental data fitting under various levels of applied forces for a 0.50 Hz excitation: (a) force-displacement; and (b) force-velocity plots.

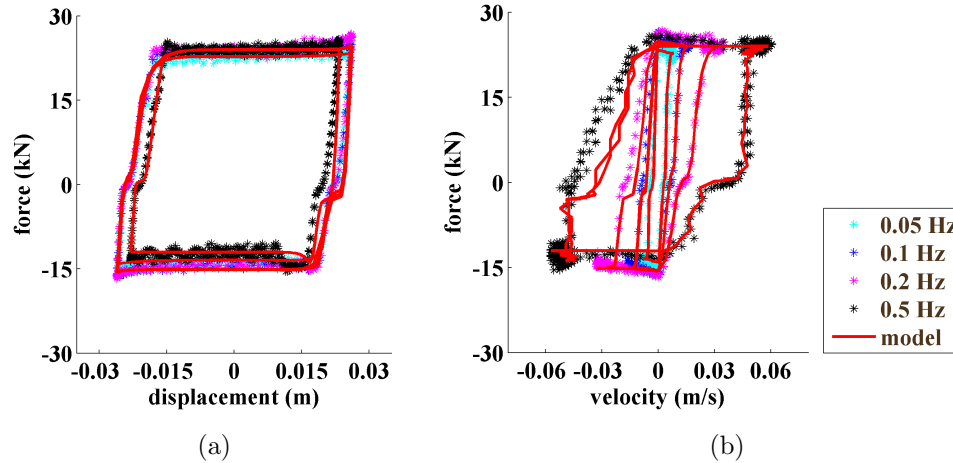


Figure 10: Experimental data fitting under various excitation frequencies for a 133 N (30 lbs) applied force: (a) force-displacement; and (b) force-velocity plots.

325 pure LuGre friction model optimized following a similar methodology used
 326 to identify the parameters for the 3-stage dynamic model. The listed RMSE
 327 confirm the performance of the 3-stage dynamic model discussed above. The
 328 pure LuGre model shows similar performance under a 53 N (12 lbs), with a
 329 substantially worst performance in the fitting to the experimental data for
 330 higher applied forces. This comparison demonstrates the necessity to still
 331 use the 3-stage dynamic model to characterize the behavior of the BRFD,
 332 due to the device's backlash.

333 Finally, a comparison is made between the hysteretic behavior of the
 334 first generation MFD and the BRFD. Figs. 11a and 11b show the modeled
 335 force-displacement and force-velocity plots of the BRFD in terms of % force,
 336 starting with an applied force of 35 N (13%). For completeness, results from
 337 various applied forces are compared against the modeled dynamic behavior

Table 4: Comparison of fitting RMSE (kN)

Force applied force	0.05 Hz		0.1 Hz		0.2 Hz		0.5 Hz	
	3-stage	LuGre	3-stage	LuGre	3-stage	LuGre	3-stage	LuGre
35 N	5.96	15.4	6.98	13.3	8.81	21.1	14.3	29.3
53 N	3.07	5.38	3.25	5.38	3.51	6.00	3.34	5.47
66 N	4.54	44.5	2.80	40.7	2.45	55.1	4.00	100
133 N	7.56	76.3	15.7	127	44.1	46.2	27.8	117
267 N	5.56	115	9.56	58.9	12.0	40.5	22.7	126

338 of the first-generation rotary damping system (the MFD) in Figs. 11c and
 339 11d. The backlash region is indicated in Figs. 11a and 11c, along with the
 340 dynamic range under its maximum applied force. The backlash of the BRFD
 341 is reduced to 2mm, from 12 mm for the MFD, while the dynamic range is
 342 increased from 5.55 kN (MFD) to 79.0 kN (BRFD). This demonstrates that
 343 the backlash effect has been substantially minimized, and that the BRFD is
 344 capable of producing substantially higher damping force.

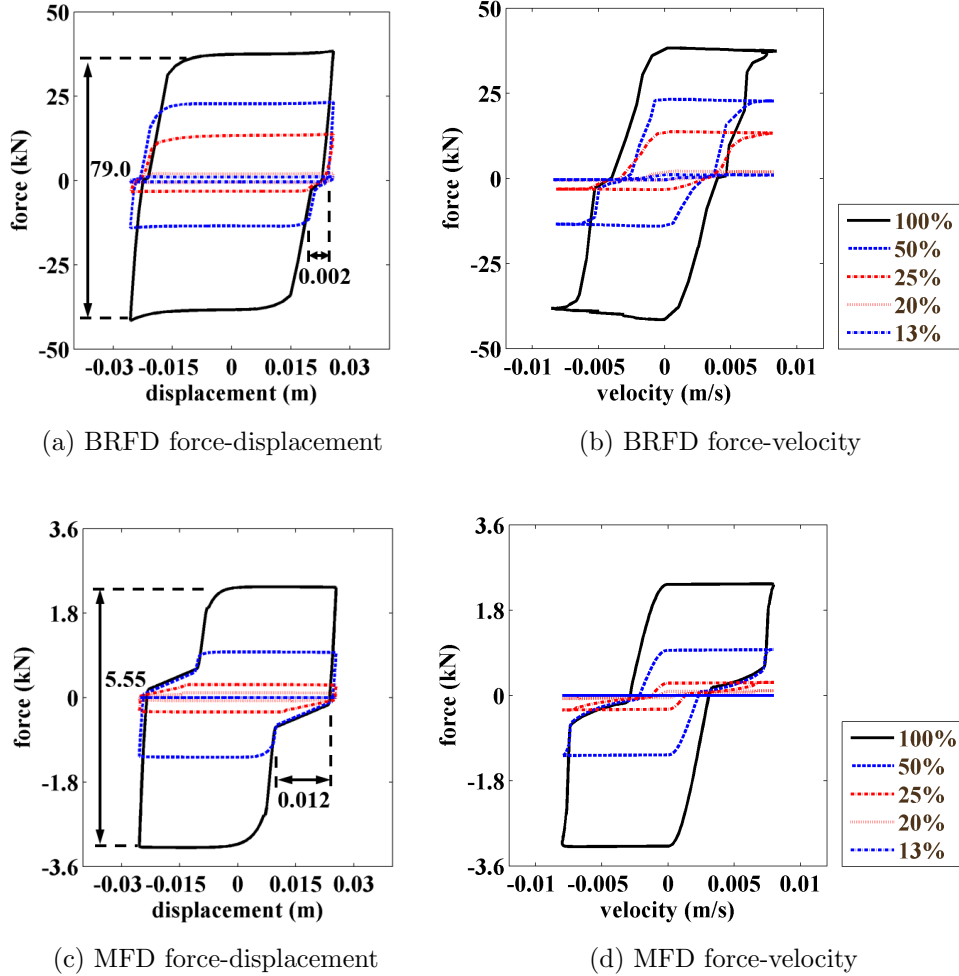


Figure 11: Modeled dynamics of the BRFD and MFD under various applied forces under a 0.05 Hz excitation of 25.4 mm (1 in) amplitude:

345 *4.5. Validation under Nonstationary Excitations*

346 The BRFD and its model are further validated using nonstationary exci-
 347 tations, consisting of two seismic excitations. The first excitation is the 1979
 348 Imperial Valley earthquake record from USGS Station 5115 and the second

349 the 1961 Hollister earthquake record from USGS station 1028. Ground dis-
350 placements were computed by double integrating the ground acceleration
351 obtained from the PEER ground motion database [42], and the maximum
352 amplitude of each ground displacements is scaled to 0.01 m (0.4 in) to match
353 the testing equipment's limitations. The BRFD was subjected directly to
354 these displacement time-histories, as the purpose of the tests was to validate
355 the model under nonstationary dynamics rather than validating damping
356 characteristics within a structural system. Acceleration and scaled displace-
357 ment time histories are shown in Fig. 12.

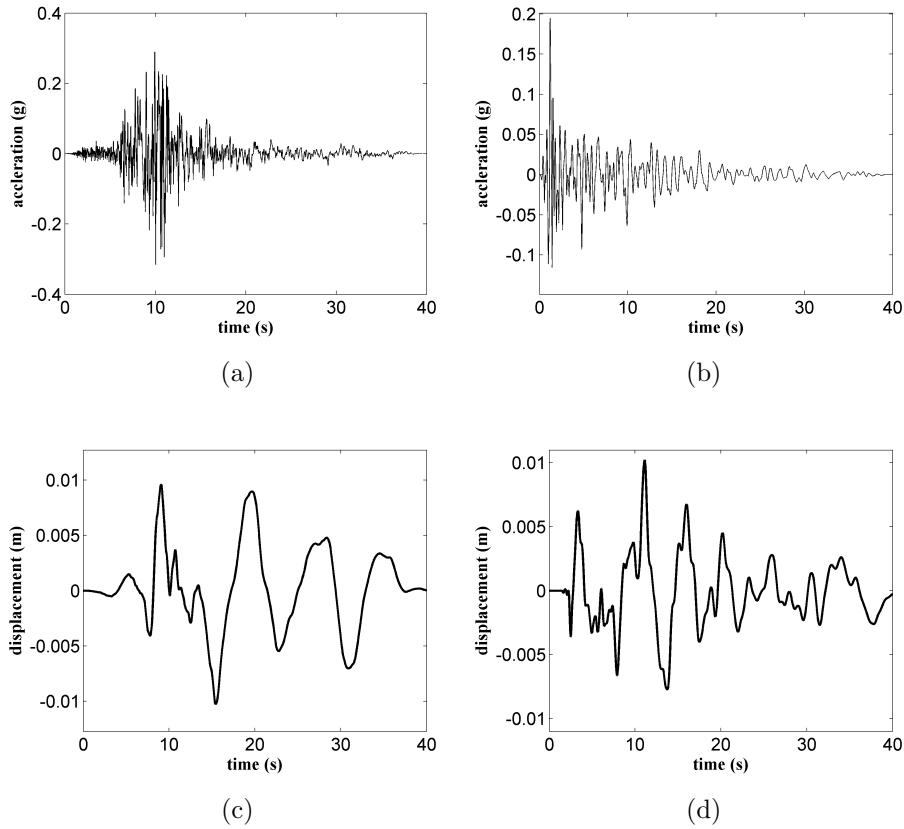
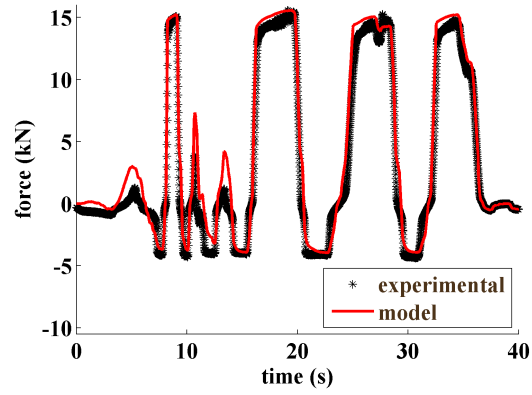


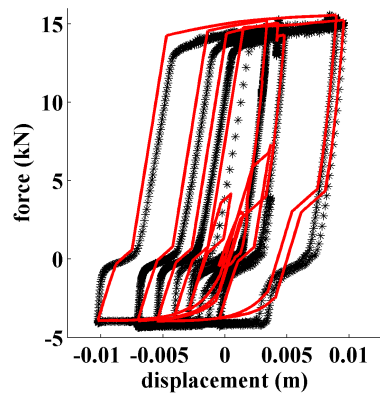
Figure 12: Earthquake excitations: (a) unscaled ground acceleration (Imperial Valley earthquake) ; (b) unscaled ground acceleration (Hollister earthquake); (c) scaled ground displacement (Imperial Valley earthquake); and (d) scaled ground displacement (Hollister earthquake).

358 The device is tested under two applied forces: 66 N (15 lb) and 133
 359 N (30 lb). Fig. 13 to 16 show the time history, force-displacement, and
 360 force-velocity plots for each seismic excitation. There is a good match of
 361 the theoretical model with the experimental data for both applied forces.
 362 A matching discrepancy is clearly observable under the Hollister earthquake

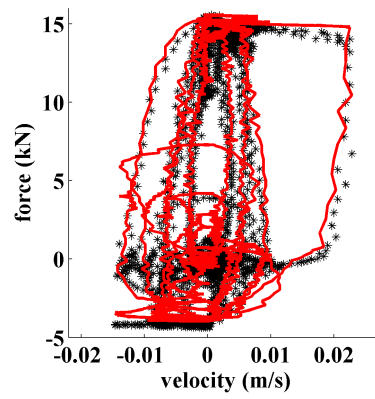
363 at around 25 sec (Fig. 15(a) and Fig. 16(a)). This is due to linear ap-
364 proximation of the damping force during a change in the rotational direction
365 of the drum where backlash is present. This overshoot is also present in
366 the Imperial Valley response, and can be observed at a small magnitude at
367 around 14 sec. This phenomenon will require further investigation, but its
368 effect could be reduced through the production of a high fidelity prototype.
369 Results from this section demonstrate that the BRFD behaves as designed
370 under nonstationary excitations.



(a)

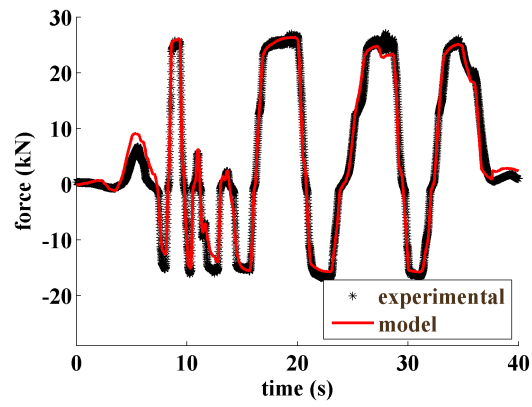


(b)

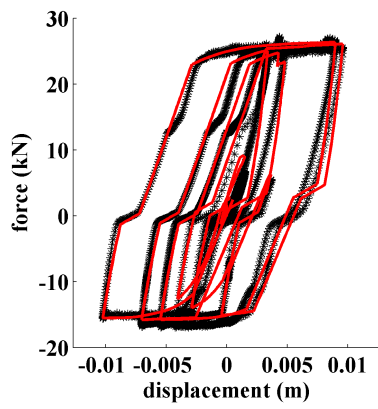


(c)

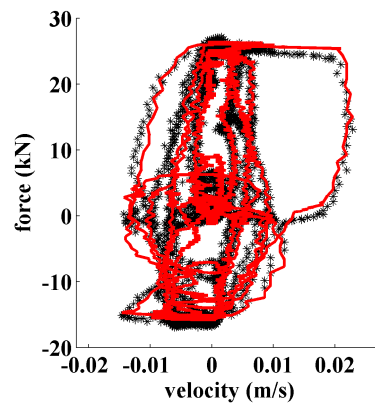
Figure 13: Imperial Valley earthquake at 66 N (15 lb): (a) time history of damping force; (b) force-displacement loop ; and (c) force-velocity loop.



(a)

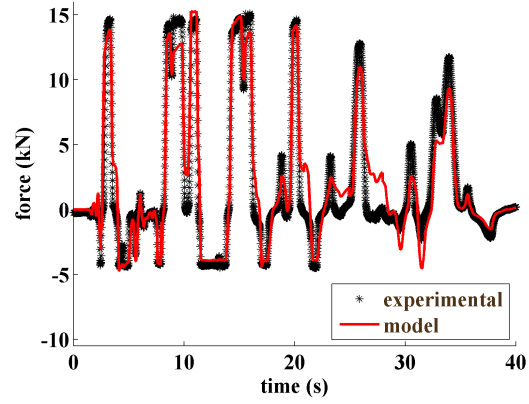


(b)

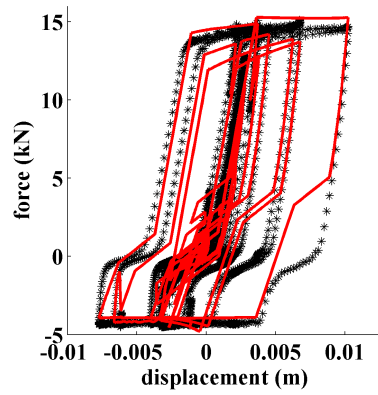


(c)

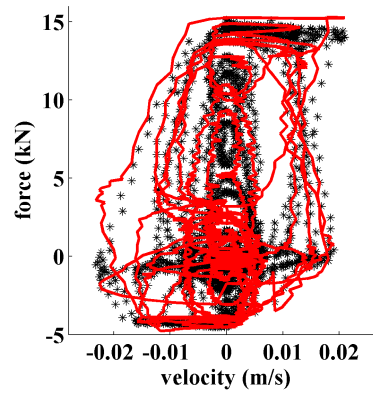
Figure 14: Imperial Valley earthquake at 133 N (30 lb): (a) time history of damping force ; (b) force-displacement loop ; and (c) force-velocity loop.



(a)

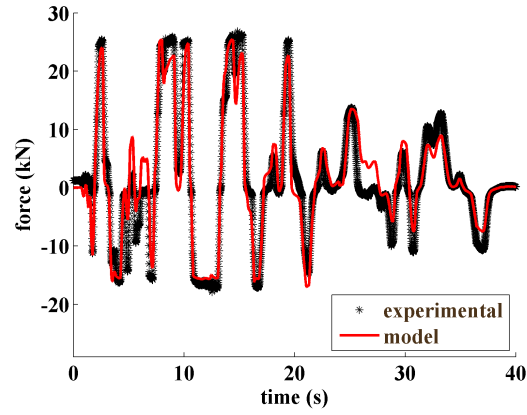


(b)

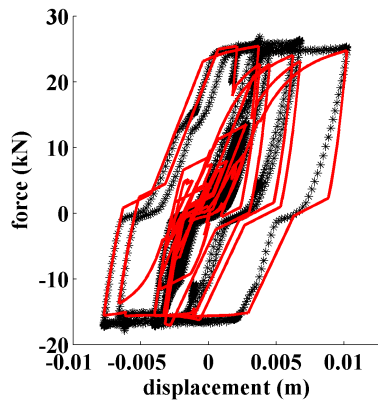


(c)

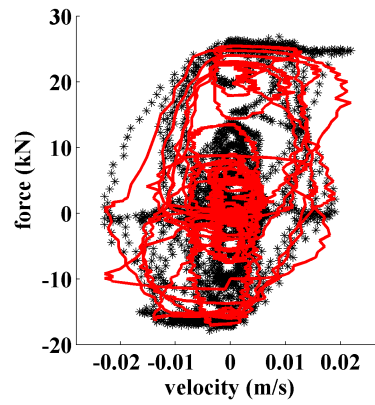
Figure 15: Hollister earthquake at 66 N (15 lb): (a) time history of damping force ; (b) force-displacement loop ; and (c) force-velocity loop.



(a)



(b)



(c)

Figure 16: Hollister earthquake at 133 N (30 lb): (a) time history of damping force ; (b) force-displacement loop ; and (c) force-velocity loop.

371 5. Summary and Conclusions

372 In this paper, a novel variable friction damper for structural control ap-
 373 plications was presented. The device, termed Banded Rotary Friction Device
 374 (BRFD), is based on the well-accepted and mature band brake technology.
 375 This makes the BRFD a mechanically robust, semi-active damping system.

376 It is capable of providing large damping forces with a substantially lower
377 applied force due to its positive servo effect.

378

379 A prototype of the BRFD was fabricated and experimentally validated.
380 The dynamic tests were conducted under harmonic loads at different frequen-
381 cies and applied forces. Results show that the prototype BRFD is capable
382 of producing a maximum 45 kN (10 kips) damping force. A 3-stage dynamic
383 model was introduced and model parameters were identified based on test
384 results. Results show that the model could be used to accurately model
385 the dynamic behavior of the device. The experimental mechanical advan-
386 tage demonstrates that the device was capable of a force amplification in
387 the range of 125-150 times the applied force. These numbers show agree-
388 ment with theoretical values. The proposed device and its model are further
389 validated using nonstationary excitations consisting of two earthquake time
390 series. Results demonstrated that the BRFD behaves as designed under non-
391 stationary excitations.

392

393 The validated prototype and friction model presented in this research
394 advances the potential for the implementation of semi-active friction devices.
395 The BRFD is the second generation of rotary damping systems designed by
396 the authors. It was specifically engineered to minimize the backlash effect
397 and increase the maximum damping force by an order of magnitude. Results
398 showed that the BRFD's has been successful at attaining both objectives,
399 therefore making it a mechanically robust device capable of high variable
400 friction force.

401 **Acknowledgement**

402 This material is based upon work supported by the National Science Foun-
403 dation under Grant no. 1300960. Their support is gratefully acknowledged.
404 Any opinions, findings, and conclusions or recommendations expressed in
405 this material are those of the authors and do not necessarily reflect the views
406 of the National Science Foundation.

407 **References**

- 408 [1] B. Spencer Jr, S. Nagarajaiah, State of the art of structural control,
409 Journal of structural engineering (2003).
- 410 [2] M. Symans, F. Charney, A. Whittaker, M. Constantinou, C. Kircher,
411 M. Johnson, R. McNamara, Energy dissipation systems for seismic ap-
412 plications: current practice and recent developments, Journal of struc-
413 tural engineering 134 (2008) 3–21.
- 414 [3] J. J. Connor, S. Laflamme, Structural Motion Engineering, Springer,
415 2014.
- 416 [4] T. E. Saaed, G. Nikolakopoulos, J.-E. Jonasson, H. Hedlund, A state-
417 of-the-art review of structural control systems, Journal of Vibration and
418 Control 21 (2015) 919–937.
- 419 [5] Y. Liu, H. Matsuhisa, H. Utsuno, Semi-active vibration isolation sys-
420 tem with variable stiffness and damping control, Journal of sound and
421 vibration 313 (2008) 16–28.

- 422 [6] W. He, A. Agrawal, K. Mahmoud, Control of seismically excited cable-
423 stayed bridge using resetting semiactive stiffness dampers, *Journal of*
424 *Bridge Engineering* 6 (2001) 376–384.
- 425 [7] J. Yang, J. Bobrow, F. Jabbari, J. Leavitt, C. Cheng, P. Lin, Full-
426 scale experimental verification of resettable semi-active stiffness dampers,
427 *Earthquake engineering & structural dynamics* 36 (2007) 1255–1273.
- 428 [8] O. Yoshida, S. J. Dyke, Seismic control of a nonlinear benchmark build-
429 ing using smart dampers, *Journal of engineering mechanics* 130 (2004)
430 386–392.
- 431 [9] B. Spencer Jr, S. Nagarajaiah, State of the art of structural control,
432 *Journal of structural engineering* 129 (2003) 845–856.
- 433 [10] T. Vesselenyi, S. Dzitac, I. Dzitac, M.-J. Manolescu, Fuzzy and neural
434 controllers for a pneumatic actuator, *International Journal of Comput-*
435 *ers, Communications and Control* 2 (2007) 375–387.
- 436 [11] A. Mehmood, S. Laghrouche, M. El Bagdouri, Modeling identification
437 and simulation of pneumatic actuator for vgt system, *Sensors and Ac-*
438 *tuator A: Physical* 165 (2011) 367–378.
- 439 [12] S. Kannan, H. M. Uras, H. M. Aktan, Active control of building seismic
440 response by energy dissipation, *Earthquake engineering & structural*
441 *dynamics* 24 (1995) 747–759.
- 442 [13] M. Lorenz, B. Heimann, V. Härtel, A novel engine mount with semi-
443 active dry friction damping, *Shock and Vibration* 13 (2006) 559–571.

- 444 [14] J. N. Yang, A. K. Agrawal, Semi-active hybrid control systems for non-
445 linear buildings against near-field earthquakes, *Engineering Structures*
446 24 (2002) 271–280.
- 447 [15] S. Narasimhan, S. Nagarajaiah, Smart base isolated buildings with vari-
448 able friction systems: H controller and saivf device, *Earthquake engi-
449 neering & structural dynamics* 35 (2006) 921–942.
- 450 [16] Y. Kawamoto, Y. Suda, H. Inoue, T. Kondo, Electro-mechanical sus-
451 pension system considering energy consumption and vehicle manoeuvre,
452 *Vehicle System Dynamics* 46 (2008) 1053–1063.
- 453 [17] C. Chen, G. Chen, Shake table tests of a quarter-scale three-storey
454 building model with piezoelectric friction dampers, *Structural Control
455 and Health Monitoring* 11 (2004) 239–257.
- 456 [18] L.-Y. Lu, G.-L. Lin, A theoretical study on piezoelectric smart isolation
457 system for seismic protection of equipment in near-fault areas, *Journal
458 of Intelligent Material Systems and Structures* 20 (2009) 217–232.
- 459 [19] O. Durmaz, W. W. Clark, D. S. Bennett, J. S. Paine, M. N. Samuelson,
460 Experimental and analytical studies of a novel semi-active piezoelectric
461 coulomb damper, in: *SPIE’s 9th Annual International Symposium on
462 Smart Structures and Materials*, International Society for Optics and
463 Photonics, 2002, pp. 258–273.
- 464 [20] Y. Xu, C. Ng, Seismic protection of a building complex using variable
465 friction damper: experimental investigation, *Journal of engineering me-
466 chanics* 134 (2008) 637–649.

- 467 [21] I. H. Mualla, B. Belev, Performance of steel frames with a new friction
468 damper device under earthquake excitation, *Engineering Structures* 24
469 (2002) 365–371.
- 470 [22] J. Pardo-Varela, J. Llera, A semi-active piezoelectric friction damper,
471 *Earthquake Engineering & Structural Dynamics* 44 (2015) 333–354.
- 472 [23] H. Dai, Z. Liu, W. Wang, Structural passive control on electromagnetic
473 friction energy dissipation device, *Thin-Walled Structures* 58 (2012) 1–8.
- 474 [24] S. Laflamme, et al., Control of large-scale structures with large uncer-
475 tainties, Ph.D. thesis, Massachusetts Institute of Technology, 2011.
- 476 [25] T. L. Karavasilis, R. Sause, J. M. Ricles, Seismic design and evaluation
477 of steel moment-resisting frames with compressed elastomer dampers,
478 *Earthquake Engineering & Structural Dynamics* 41 (2012) 411–429.
- 479 [26] Y. Chae, J. M. Ricles, R. Sause, Modeling of a large-scale magneto-
480 rheological damper for seismic hazard mitigation. part i: Passive mode,
481 *Earthquake engineering & structural dynamics* 42 (2013) 669–685.
- 482 [27] L. Cao, A. Downey, S. Laflamme, D. Taylor, J. Ricles, Variable friction
483 device for structural control based on duo-servo vehicle brake: Modeling
484 and experimental validation, *J. Sound and Vibration* (2015).
- 485 [28] Rauscher, Winch, 1922. US Patent 1,413,292.
- 486 [29] C. A. Johnson, L. H. Lucker Jr, Mooring apparatus for floating vessels,
487 1984. US Patent 4,446,807.

- 488 [30] D. S. Han, G. J. Han, D. H. Choi, A study on durability enhancement
489 of band brake for mooring winch, in: *Advanced Materials Research*,
490 volume 201, Trans Tech Publ, 2011, pp. 314–317.
- 491 [31] B. R. E. G. . Co., data sheet: Bermskerl 4500, 1640 Shanahan Drive,
492 South Elgin, IL 60177., 2013.
- 493 [32] D. P. Taylor, Toggle brace dampers: A new concept for structural
494 control, in: *Advanced technology in structural engineering: Proc.*, 2000
495 Structures Congress and Exposition, 2000.
- 496 [33] M. C. Constantinou, P. Tsopelas, W. Hammel, A. N. Sigaher, Toggle-
497 brace-damper seismic energy dissipation systems, *Journal of Structural*
498 *Engineering* 127 (2001) 105–112.
- 499 [34] A. K. Baker, *Industrial brake and clutch design*, Pentech Press, 1992.
- 500 [35] E. A. Avallone, T. Baumeister, A. M. Sadegh, *Marks' standard hand-*
501 *book for mechanical engineers*, volume 9, McGraw-Hill New York, 1996.
- 502 [36] H. Olsson, K. J. Åström, C. Canudas de Wit, M. Gäfvert, P. Lischinsky,
503 Friction models and friction compensation, *European journal of control*
504 4 (1998) 176–195.
- 505 [37] F. Altpeter, *Friction modeling, identification and compensation* (1999).
- 506 [38] C. C. De Wit, P. Lischinsky, Adaptive friction compensation with par-
507 tially known dynamic friction model, *International journal of adaptive*
508 *control and signal processing* (1998) 65–80.

- 509 [39] A. Shiriaev, A. Robertsson, R. Johansson, Friction compensation for
510 passive systems based on the lugre model, in: Lagrangian and Hamilto-
511 nian Methods for Nonlinear Control 2003: A Proceedings Volume from
512 the 2nd IFAC Workshop, Seville, Spain, 3-5 April, 2003, Elsevier, 2003,
513 p. 159.
- 514 [40] P. Lischinsky, C. Canudas-de Wit, G. Morel, Friction compensation for
515 an industrial hydraulic robot, *Control Systems, IEEE* 19 (1999) 25–32.
- 516 [41] S. Laflamme, J. Slotine, J. Connor, Wavelet network for semi-active
517 control, *Journal of Engineering Mechanics* 137 (2011) 462–474.
- 518 [42] PEER, Peer, pacific earthquake engineering research center, 2010.